



The interaction of a cylindrical shock wave segment with a converging–diverging duct

B. B. Ndebele¹ · B. W. Skews¹

Received: 5 March 2018 / Revised: 28 December 2018 / Accepted: 31 December 2018 / Published online: 31 January 2019
© Springer-Verlag GmbH Germany, part of Springer Nature 2019

Abstract

In this study, we present the results of an investigation of the propagation of cylindrical shock wave segments in converging–diverging channels. Three planar-symmetric channels were used: two formed from a pair of walls with circular wall profiles (radii 150 mm and 225 mm) and a third following a third-order-polynomial profile. In contrast to the circular walls, which are convex, the polynomial wall has both convex and concave curved sections. A plane shock was generated using a conventional shock tube after which a 165-mm-radius cylindrical shock segment was formed by allowing the plane shock to pass through a circular arc-shaped annular space. This shock was then allowed to propagate in the converging–diverging channel formed from the two walls described earlier. The resulting shock evolution was captured using a z -type schlieren technique. Whitham’s geometric shock dynamics (GSD) and computational fluid dynamics (CFD) were used to create numerical models of the shock’s propagation. Comparisons between the three methods (experiment, CFD, and GSD) were made. In general, qualitative agreements between the three methods were observed (with slight discrepancies). For example, a shock with an initial Mach number of 1.37 interacting with a 150-mm-radius wall exhibited high curvature at the shock’s central position towards the channel’s throat (as observed in experiment), an observation which was not replicated by either CFD or GSD. Quantitatively, there were significant differences (before accounting for experimental errors). On comparing centreline shock Mach numbers between the three methods, CFD results were closer to experimental results, while GSD results were consistently higher but within the experimental data error bounds. However, the general trend was the same in all three, i.e., the shock strengthens and weakens in the converging and diverging sections, respectively.

Keywords Cylindrical shock wave · Converging–diverging duct · Diffraction · Reflection · Geometric shock dynamics

List of symbols

(α, β)	Coordinates on a curvilinear coordinate system	f_1, f_2	Property value (e.g., density) for a fine and course mesh (relatively), respectively
(x, y)	Coordinates on a Cartesian plane	M	Shock Mach number
ϵ_M, ϵ_P	Error in shock Mach number and position, respectively	M_0	Initial shock Mach number
$\eta(M)$	Modification factor of Whitham’s theory	p	Position of probe point
γ	Ratio of specific heat capacities	r	Shock radius, or ratio between course and fine mesh sizes
θ	Shock orientation	t	Time
\mathbf{n}_r	Normal on the shock front	u, v	x and y component of velocity
A	Channel cross-sectional area	GCI	Grid Convergence Index
a_0	Speed of sound ahead of the shock		

Communicated by M. Brouillette and A. Higgins.

✉ B. B. Ndebele
brightndebele@hotmail.com

¹ University of the Witwatersrand, 1 Jan Smuts Av.
Braamfontein, Johannesburg 2000, South Africa

1 Introduction

Shock waves propagating in channels occur in different areas of our environment. These may be accidental or by design. Consider underground gas pipelines; in the event of an accident, earthquake or any incident that causes inadvertent

explosions, shock waves may propagate in these underground channels. A similar example can be made of coal dust in mines where the dust acts as a fuel. Stray sparks from mining equipment may act as an ignition source, resulting in an explosion.

Several researchers have investigated the propagation of plane shock waves under different conditions [1]. Here, we consider the propagation of a cylindrical shock wave segment in a converging–diverging channel. Further to that, Whitham’s geometric shock dynamics (GSD) and CFD are used to model the said propagation and results compared to experimental investigations.

2 Geometric shock dynamics

Consider a shock wave propagating in a channel with a slowly varying cross-sectional area. Chester [2], Chisnell [3], and Whitham [4] showed that the shock Mach number and the cross-sectional area can be related by (1). This relation is called the CCW relation. In general, the expression shows that an increase in the channel’s cross-sectional area ($dA > 0$) results in a decrease in shock Mach number ($dM < 0$).

$$\frac{2M dM}{(M^2 - 1)K(M)} + \frac{dA}{A} = 0 \tag{1}$$

with

$$K(M) = \left[2(2\mu + 1 + M^{-2})^{-1} \left(1 + \frac{2}{\gamma + 1} \frac{1 - \mu^2}{\mu} \right)^{-1} \right]$$

where

$$\mu(M) = \left(\frac{(\gamma - 1)M^2 + 2}{2\gamma M^2 - (\gamma - 1)} \right)^{\frac{1}{2}}$$

A major assumption that was made by all three researchers in deriving (1) is the so-called free propagation assumption stating that the behaviour of the shock front was independent of post-flow conditions. While this assumption works well for relatively strong shocks ($M > 2$), it is not plausible for weak shocks where re-reflected waves may catch up with the shock front [4]. Skews [5] and Bryson and Gross [6] illustrated this in their experiments. In light of that weakness, Milton [7] accounted for post-shock condition in strong shocks and Itoh et al. [8] generalised this over the whole range of shock Mach numbers (2) by inclusion of the $\eta(M)$ term. On integrating (1) or (2), the explicit form of the area–Mach number relation ($A = A(M)$) is arrived at.

$$\left(\frac{2M}{(M^2 - 1)K(M)} + \frac{\eta(M)}{M} \right) dM + \frac{dA}{A} = 0 \tag{2}$$

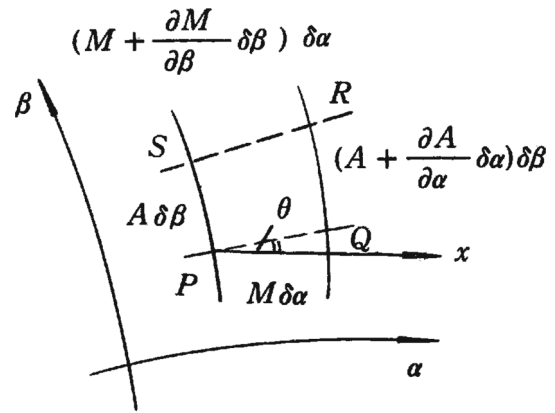


Fig. 1 Curvilinear coordinate system for deriving Whitham’s model

with

$$\eta(M) = \left(1 - \frac{M_0^2}{M^2} \right) \frac{(F + 2B)E}{(M^2 - 1)BD} + \frac{1}{2} \ln \left(\frac{A_0}{A} \right) + \frac{D^{\frac{3}{2}}(M^2 + 1) + 4(M^2 - 1)^2 F}{(M^2 - 1)DE}$$

$$QB = 2\gamma M^2 - (\gamma - 1)$$

$$C = (\gamma - 1)M^2 + 2$$

$$D = BC$$

$$E = 2(M^2 - 1) + \sqrt{D}$$

$$F = (\gamma - 1)(1 + \gamma M^4)$$

Following on the CCW relation, Whitham considered an arbitrarily shaped shock propagating in a channel with arbitrarily shaped walls. Whitham modelled the shock using a curvilinear coordinate system (α, β) (Fig. 1). Lines of constant α represent successive shock fronts, while constant β represents rays; hence, Fig. 1 is called a ray-shock diagram. Terminal rays are the walls’ profile, while intermediate rays can be viewed as pseudo-walls. Using Fig. 1, Whitham showed that the geometric relations governing the shock are (3) and (4) which translate to (5) in characteristic form.

$$\frac{\partial \theta}{\partial \beta} - \frac{1}{M} \frac{\partial A}{\partial \alpha} = 0 \tag{3}$$

$$\frac{\partial \theta}{\partial \alpha} + \frac{1}{A} \frac{\partial M}{\partial \beta} = 0 \tag{4}$$

$$\left(\frac{\partial}{\partial \alpha} \pm c \frac{\partial}{\partial \beta} \right) \left(\theta \pm \int \frac{dM}{Ac} \right) = 0 \tag{5}$$

$$c = \sqrt{\frac{M}{A'(M)A(M)}} \tag{6}$$

θ represents the shock’s orientation with respect to the x -axis. An important prediction made by (5) is that as the shock prop-

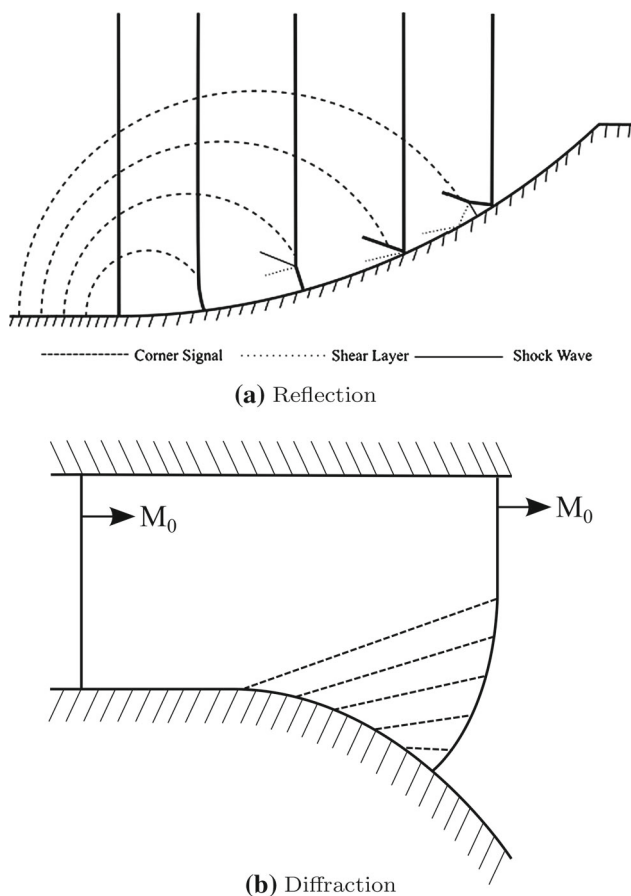


Fig. 2 Reflection and diffraction on walls with slowly varying gradient

agates along the channel, waves, with speed c , also propagate up or down along the shock. It is these waves that transfer information for the shock’s shape and strength to change.

Consider Fig. 2a, b which shows plane shock reflection and diffraction, respectively. In both cases, the upper wall is plane and perpendicular to the shock. Because the upper wall is straight, there are no waves propagating down along the shock. However, the curvature of the bottom walls causes wall disturbances to propagate up along the shock. According to Whitham, these waves propagate at a speed given by (6), from which we see that the speed depends on both the channel cross-sectional area and the shock Mach number.

Figure 2a, b is akin to an accelerating and decelerating piston, respectively. In line with this analogy, the disturbance waves generated in Fig. 2a, b are, correspondingly, compressive and expansive. If it is imagined that these waves are discrete, then $c_1 < c_2 < \dots < c_n$ and $c_1 > c_2 > \dots > c_n$ for Fig. 2a, b, respectively, where c_1 is the first disturbance, c_2 the second, and so on. Consequently, for Fig. 2a, successive waves grow stronger and eventually may coalesce to form a shock–shock, a discontinuity on the shock front. In Fig. 2b, a non-centred expansion fan results in curving the shock into a smooth continuous profile.

Henshaw et al. [9] presented a numerical technique for calculating the evolution of the shock front using GSD. The solution scheme relies on a transformation from the curvilinear coordinate system to the rectangular system along a ray. Whitham [4] showed that this transformation results in (7).

$$\frac{\partial x}{\partial \alpha} = M \cos \theta, \quad \frac{\partial y}{\partial \alpha} = M \sin \theta \tag{7}$$

For brevity, (7) are written in vector form as (8), with $\mathbf{x} = (x, y)$ and $\alpha = a_0 t$. The partial derivative is then discretised as in (9) where i refers to the different β coordinates.

$$\frac{\partial \mathbf{x}(\beta, t)}{\partial t} = a_0 M(\beta, t) \mathbf{n}(\beta, t) \tag{8}$$

$$\mathbf{x}_i(t + \Delta t) = \mathbf{x}_i(t - \Delta t) + 2\Delta t M_i(t) \mathbf{n}_i(t), \tag{9}$$

$$i = 1, \dots, N$$

The shock’s Mach number is solved for, using a discretised form of (1) (or 2). Equation (2) was used in this investigation. The index i refers to the shock discretisation on the β axis. Complementing (7) and (1) (or 2) are the initial conditions (the initial shock Mach number and shock front shape) and the boundary conditions (that the shock front is always perpendicular to the bounding walls). The leap-frog numerical scheme can then be used to determine the shock front’s shape and shock Mach number and their variation with time. In this investigation, Henshaw et al.’s numerical scheme was implemented in MATLAB. The leap-frog scheme was implemented, with a time step of 10^{-8} s. Henshaw et al.’s criteria for point deletion and addition were used in order to maintain sufficient shock resolution in compressive and expansive regions, respectively.

3 Current problem

Of concern in this paper is the propagation of cylindrical shock waves in converging–diverging channels. Because the wall shape changes, Whitham’s theory predicts that there will be disturbance waves propagating up and down along the cylindrical shock front. Further to that, since the shock’s Mach number depends on the shock’s radius, the speed of these disturbance waves will also be variable [10]. It is not clear how these effects together with channel area variation will affect the shock’s behaviour and the evolution of the shock front.

As such, Whitham’s theory is used to model the evolution of the shock front as it interacts with the channel’s walls. The results of the model are then compared to experimental data. Figure 3a, b shows the two types of channel walls that were investigated. The tangents in Fig. 3a illustrate the variation in wall angle from the shock’s perspective, i.e., the cylindrical

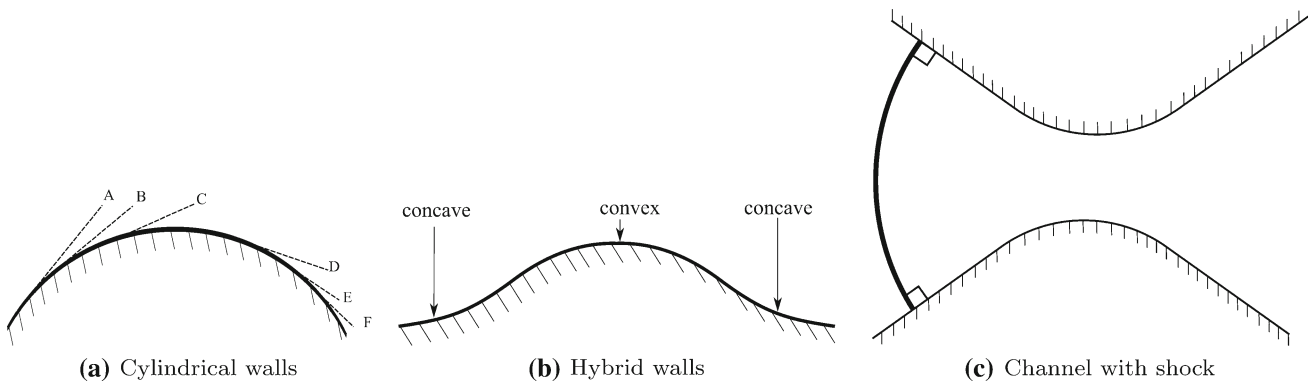


Fig. 3 Types of walls used to define the channels through which the shock propagates

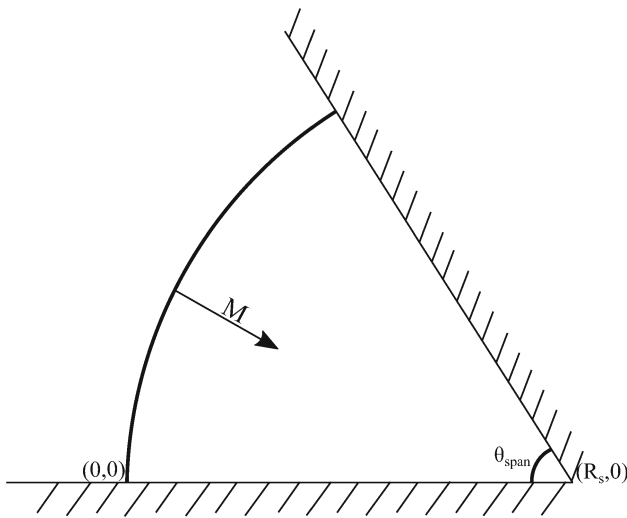


Fig. 4 Shock dimensions: $R = 165 \text{ mm}$, $\theta_{\text{span}} = 55^\circ$

channel walls are similar to the case illustrated by Fig. 2b. The hybrid wall is a mixture of concave and convex walls (Fig. 2a, b). Equation (10) (in mm) defines the hybrid wall profile.

$$y = \begin{cases} 1.5 \times 10^{-3}x^2 + 3.933 \times 10^{-1}x + 70.006, & x < 38.5 \\ -1 \times 10^{-5}x^3 - 1.7 \times 10^{-3}x^2 + 1.05x + 38.40, & \\ 1.1 \times 10^{-3}x^2 - 9.582 \times 10^{-1}x + 245.64, & x > 221.5 \end{cases} \quad (10)$$

The dimensions of the cylindrical shock investigated are shown in Fig. 4. Motivating these dimensions are the experimental apparatus, to be discussed in Sect. 4.2.

4 Investigation methods

Three methods were used to investigate the interaction between a 165-mm-radius shock segment and a converging–diverging duct: CFD, experiments, and Whitham’s GSD. In

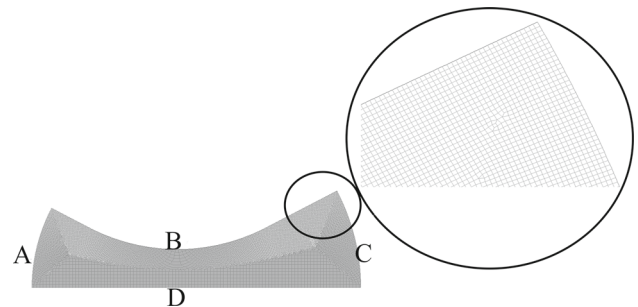


Fig. 5 Typical mesh on a 150-mm-radius channel

the next two sections, we present details for the CFD and experimental set-up. Whitham’s GSD was applied following the method described by Henshaw et al. [9].

4.1 CFD set-up

ANSYS Fluent 15.0.0 was used for all CFD simulation. This section summarises the settings used. All simulations were two dimensional with a plane of symmetry along the channel centreline. This symmetry was used to halve the simulation domain.

ANSYS meshing was used to create a rectangular dominant mesh (Fig. 5) with an element size of 0.15 mm. For the specific case shown in Fig. 5, the result was a grid with 46,733 cells, 94,094 faces, and 47,362 nodes. Edges A, B, C, and D were defined as a pressure inlet, a wall, outlet, and a symmetry plane, respectively.

In Fluent, a density-based solver was implemented on the mesh created (typically as in Fig. 5). Typical solver settings are shown in Table 1 for a Mach 1.5 incident shock. The fluid domain was initialised to ambient conditions. Custom field functions (11) were created for the inlet conditions and patched accordingly, to the pressure-inlet boundary condition.

Table 1 Fluent settings for the simulation of a 165-mm-radius cylindrical shock interacting with a 150-mm-radius wall

Energy	On
Viscous model	Inviscid
Material	Air (as an ideal gas)
Boundary conditions	
Pressure inlet	
Total pressure	378,511.3 Pa
Supersonic gauge pressure	256,400 Pa
Total temperature	475.72 K
Methods	
Formulation	Implicit
Flux type	Roe-FDS
Spatial discretisation	
Gradient	Least squares cell based
Flow	Second-order upwind
Transient formulation	Second-order implicit
Courant number	1
All residuals	1×10^{-5}
Time step	1×10^{-8} s

Initial shock Mach number is 1.7; ambient pressure and temperature are 80,000 kPa and 291.85 K, respectively

$$\begin{aligned}
 u &= 314.26 \cos \theta \\
 v &= 314.26 \sin \theta \\
 \theta &= \tan^{-1} \left(\frac{Y}{X - 0.165} \right)
 \end{aligned}
 \tag{11}$$

A density-based adaptive refinement method was implemented in order to achieve fine shock front resolution. The solver was set to refine the mesh where the spatial density gradients are greater than 0.015 kg m^4 and coarsen when less than 0.01 kg m^4 . Should the density gradient be intermediate, the mesh remains unmodified. The maximum level of refinement was set to four, which means that the concerned cell is split by a factor of 2^4 .

Mesh independence

A grid independence study was performed using the 150-mm-radius wall. Two meshes with nominal sizes of 1 mm and 0.5 mm were used for this study. Roache’s method [11] for analysing grid convergence was followed. The Grid Convergence Index (GCI) is shown in (12) where the grid ratio, r , is determined based on the dynamically adapted mesh, and $p = 2$ for a second-order simulation.

$$\text{GCI} = \frac{3|\epsilon|}{r^p - 1} \quad \text{where } \epsilon = \frac{f_2 - f_1}{f_1}
 \tag{12}$$

Table 2 Solution details at 310 μs

Case	Δ	# Elem*	# Elem	Velocity (m s^{-1})	GCI
A	0.5	46,733	162,566	322.420	–
B	1.0	11,735	15,590	321.582	0.26%

Flow Mach number was extracted at the arbitrary coordinates (125, 0) mm. Δ is the nominal mesh size in mm, # Elem* is the number of elements in the mesh before adaptation, and # Elem is the number of elements at 310 μs

Table 3 Solution details at 200 μs

Case	Δ	# Elem*	# Elem	Velocity (m s^{-1})	GCI
A	0.5	46,733	106,010	364.703	–
B	1.0	11,735	14,303	363.592	0.30%

Flow Mach number was extracted at the arbitrary coordinates (125, 0) mm. Δ is the nominal mesh size in mm, # Elem* is the number of elements in the mesh before adaptation, and # Elem is the number of elements at 200 μs

Tables 2 and 3 show the results of the GCI calculation. The results show negligible difference between the results using a 1-mm grid and a 0.5-mm grid. It can, therefore, be assumed that the solutions that follow are independent of the grid.

4.2 Experimental set-up

The Large-Scale Diffraction Shock Tube (LSDST) designed by Lacovig [12] was used for the experimental investigations. The tube uses air as a working fluid, with the driven section open to ambient temperature and pressure. Its dimensions are shown in Table 4. The LSDST produces plane shock waves which, for the purposes of this study, must be transformed into cylindrical shocks. This is achieved by use of a modular rig designed by Skews et al. [13]. Because the rig is modular, it can be used to investigate various channels by swapping test pieces.

Figure 6 shows an image and schematic of the said test rig. The cylindrical shock generated by the test section has a radius of 465 mm and a span of 55° . With a propagation chamber of 300 mm, the effective shock radius, on interaction with the test-piece, is 165 mm. Two pressure transducers connected to the LSDST allow for the estimation of the shock’s Mach number on entering the test rig. Using (1) (or 2), the shock’s initial Mach number when it interacts with the test-piece can be calculated. We used (2).

A standard schlieren system was used for flow visualisation. Figure 7 is a schematic of the set-up. A Photron camera, set at 60,000 frames per second and a shutter speed of 1 μs , was used to capture the images. A Megaray MR2175LAB light source was used for providing light. Two parabolic mir-

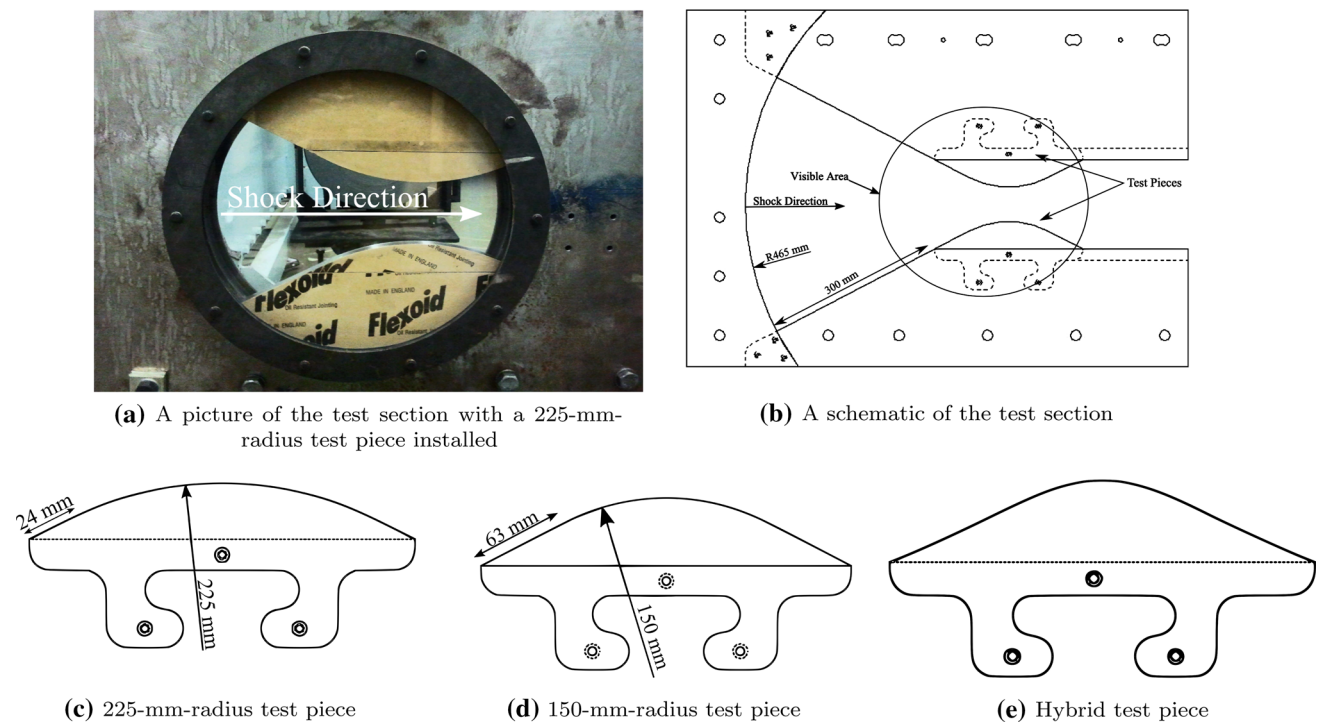


Fig. 6 Experimental apparatus for the production of cylindrical shock waves

Table 4 Shock tube dimensions

Driver section length	2 m
Driven section length	6 m
Channel cross section	450 mm × 100 mm

rors with focal lengths of 1840 mm were used to produce the required parallel light beam.

5 Results and discussion

5.1 CFD results

Figure 8 shows a qualitative summary of the CFD results illustrated using the 150-mm-radius case. In the converging section of the channel, the shock is seen to diffract along the convex wall (Fig. 8a, b); this results in a shock front that is partitioned into three sections (Fig. 9). The middle section maintains its cylindrical profile and continues to converge on itself. The result is the formation of a multi-wave system (Fig. 8c, d) which is similar to a Mach reflection. In Fig. 8e, f, the wave system reflects off of the bounding walls. Similar behaviour can be observed in the experimental results that follow. In Sect. 5.3, CFD and experimental results are compared.

5.2 Experimental results

Figures 10, 11, 12, 13, and 14 show some of the experimental results from the shock tube experiments. The shock waves investigated had initial shock Mach numbers between 1.25 and 1.37. In all the cases investigated, the shock front maintains a uniform profile. In general, the convex-cylindrical shock transforms to a planar shock close to the channel throat and then becomes concave curved in the diverging section.

As illustrated in Fig. 9, the shock front is split into three regions by disturbance waves propagating up and down along the shock (as has already been noted in Sect. 5.1). The middle portion (which maintains a converging cylindrical shape) continues to accelerate towards its focal point. It was thought, therefore, that this would result in the formation of discontinuities on the shock front owing to the strengthening of disturbances propagating on the shock front. This null result is possible if the disturbance waves from the channel walls deform the shock front such that it no longer is cylindrical when the focal point is reached.

While maintaining a uniform shock front, in the channel defined by 150-mm walls, waves can be observed protruding behind the shock—consider Figs. 11d and 12d–l which exhibit signs of a possible discontinuity forming. Figure 12h shows a multi-wave system; here, we avoid calling it multi-shock (or discontinuity) as it is possible that they are compression waves instead. Furthermore, Figs. 10, 11, and 12 also illustrate that the shock's Mach number plays a role

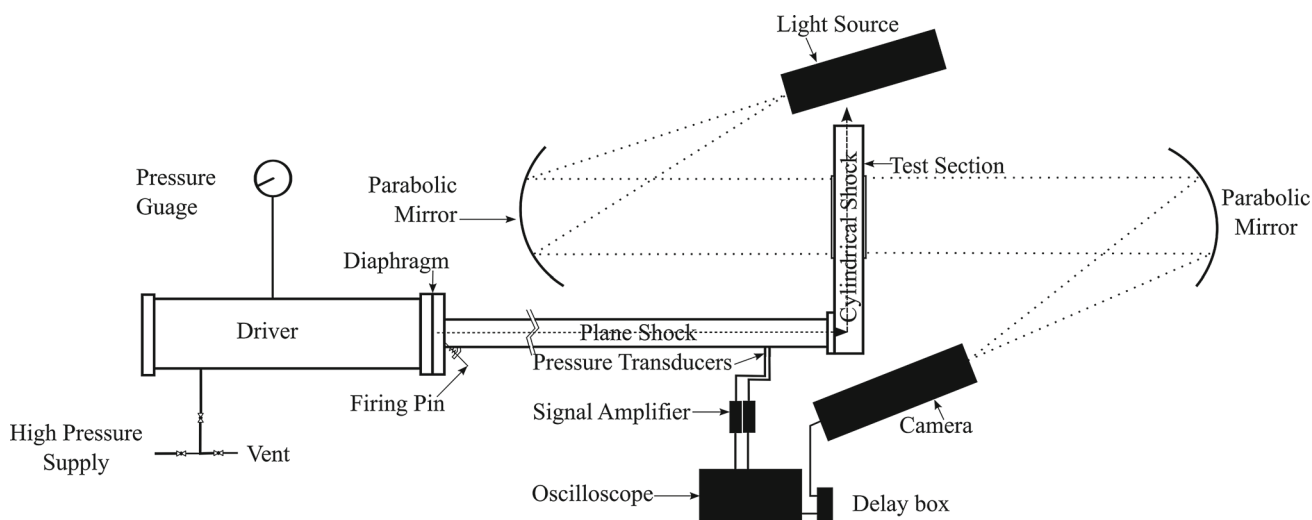


Fig. 7 Plan view of the schlieren set-up and auxiliary connections for the shock tube

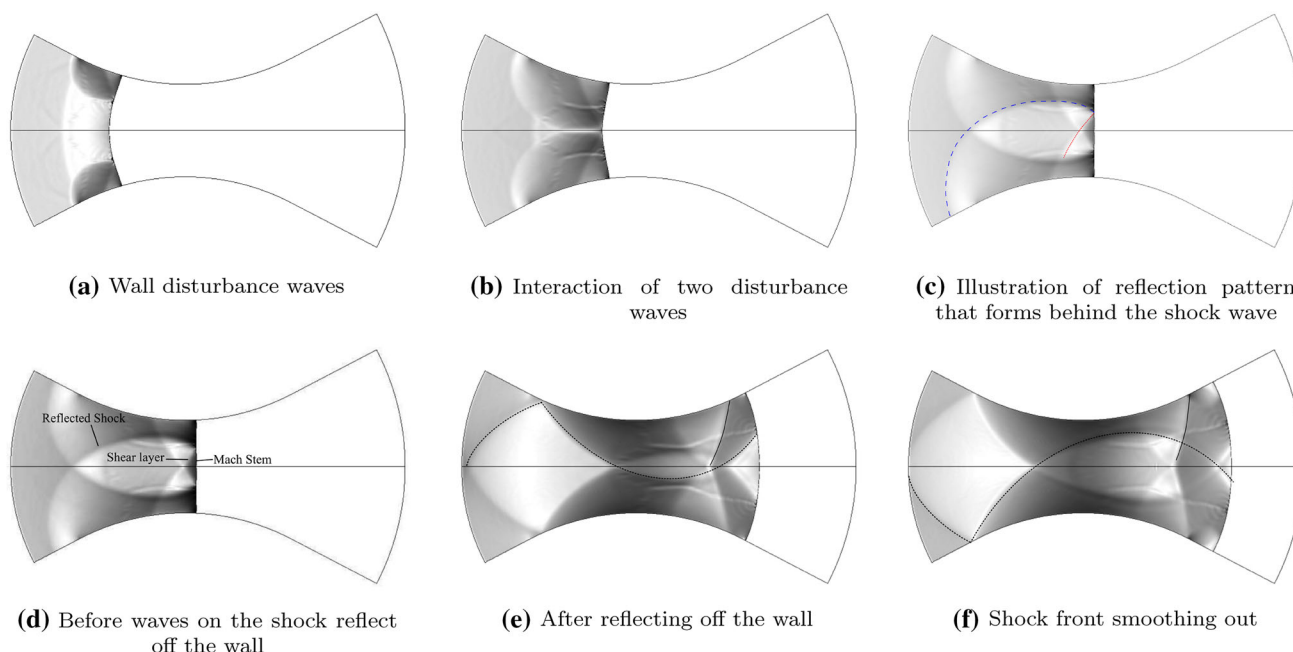


Fig. 8 CFD simulation of a shock propagating in a 150-mm-radius channel

in the formation of this multi-wave system, i.e., the waves forming this system become stronger with increasing shock Mach number.

In Fig. 12i, this multi-wave system reflects off the channel’s walls. This reflection shows that the two features behind the shock should be classified as two distinct features. On reflection, one of the features remains attached to the shock front, while the other remains behind (Fig. 12j, k).

In the channel formed from hybrid walls, the shock has both compressive and expansive disturbance waves propagating on its front. The concave and convex sections of the profile induce compressive and expansive disturbance waves,

respectively. That, combined with a converging cylindrical shock and a narrower channel throat, results in similar but sharper effects compared to the channel with 150-mm walls.

The effect of wall radius can be seen by comparing Figs. 10 and 12. The difference in incident Mach number between the two cases is 0.2, yet the differences in outlet shock curvature are significant. The 225-mm-radius wall produces a more planar-looking shock compared to the 150-mm-radius wall. A decrease in wall radius corresponds to a reduction in the minimum channel cross-sectional area and inversely an increase in Mach number as illustrated by the area Mach number relation. It follows therefore that the channel

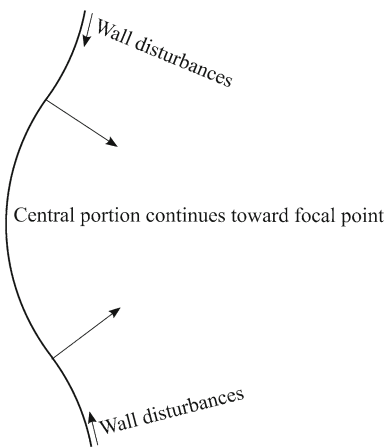


Fig. 9 Shock front partitioned into three regions

with 150-mm-radius walls produces stronger wall disturbance waves than the channel defined by 225-mm-radius walls (compare Figs. 10c and 12e). As a consequence, the 150-mm-radius channel produces a more curved shock with

its three sections well defined. However, a more apt comparison would have been made if the perimeter of the test pieces' circular profile had the same in both the 225-mm and 150-mm pieces.

5.3 Comparison between CFD and experiment

Figure 15 is a comparison of shock profiles derived from CFD and experiment. Figure 15a–c corresponds to shocks at times 140 μ s, 200 μ s, and 160 μ s, respectively. Of the three cases, the shock in the polynomial wall channel shows major discrepancies; the experiment-derived profile has high curvature towards its centre (see also Fig. 13g), which CFD does not adequately reproduce.

Shock Mach numbers along the symmetry plane are shown in Fig. 16a–c. The error estimates associated with experimental measurements are as a result of apparent shock thickness (Sect. 5.4). Within experimental uncertainty, CFD and experimental values are consistent with each other except for the polynomial wall profile. The reason behind this discrepancy

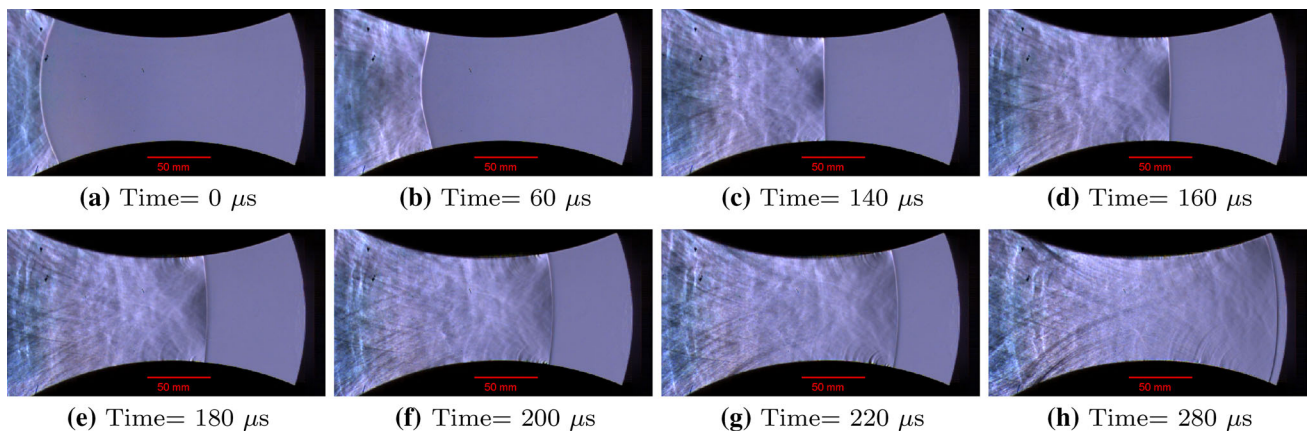


Fig. 10 Propagation of a shock with an initial shock Mach number of 1.37 in a channel with 225-mm-radius walls

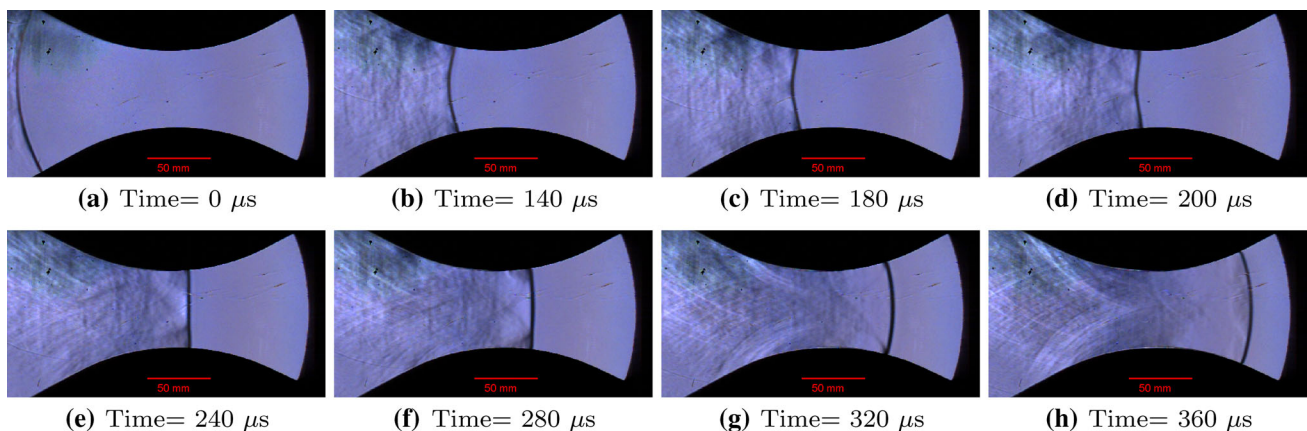


Fig. 11 Propagation of a shock with an initial shock Mach number of 1.25 in a channel with 150-mm-radius walls

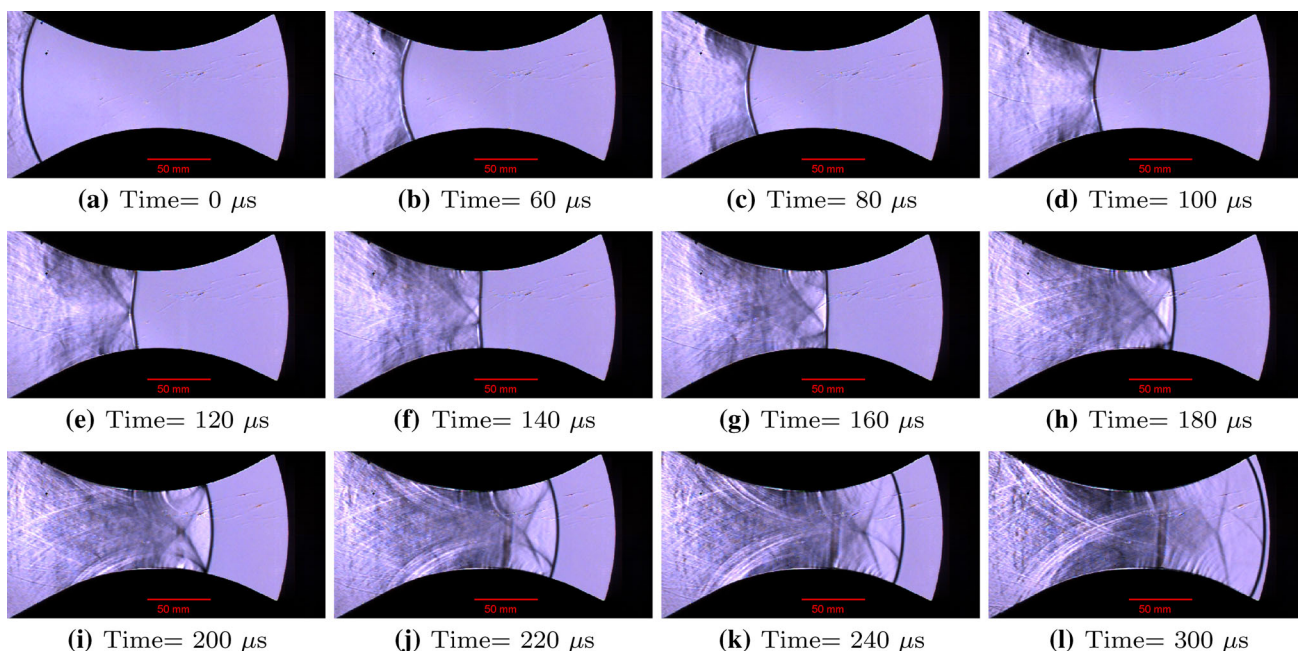


Fig. 12 Propagation of a shock with an initial shock Mach number of 1.39 in a channel with 150-mm-radius walls

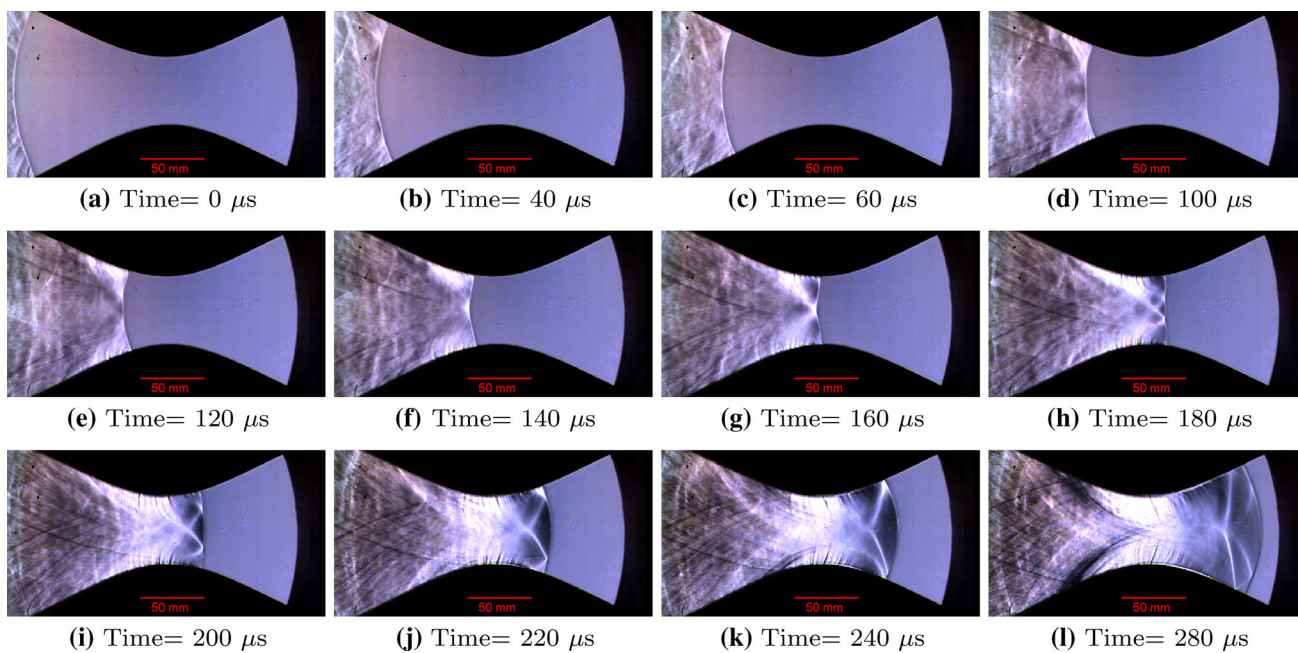


Fig. 13 Propagation of a shock with an initial shock Mach number of 1.39 in a channel with hybrid walls

is not clear; the only difference between the circular and polynomial wall profiles is the initial convex section in the latter. Owing to this convex section, the polynomial wall profile causes compressive wall disturbances to propagate along the shock front. However, this alone cannot account for the discrepancy observed.

5.4 Error analysis

In this section, we determine the error associated with the centreline shock Mach numbers illustrated in Fig. 16 and later on in Sect. 5.6. An elementary method was employed in calculating shock speed, i.e., the ratio of shock displacement with time. Shock positions were extracted from the captured images (Figs. 10, 11, 12, 13, and 14), for which it

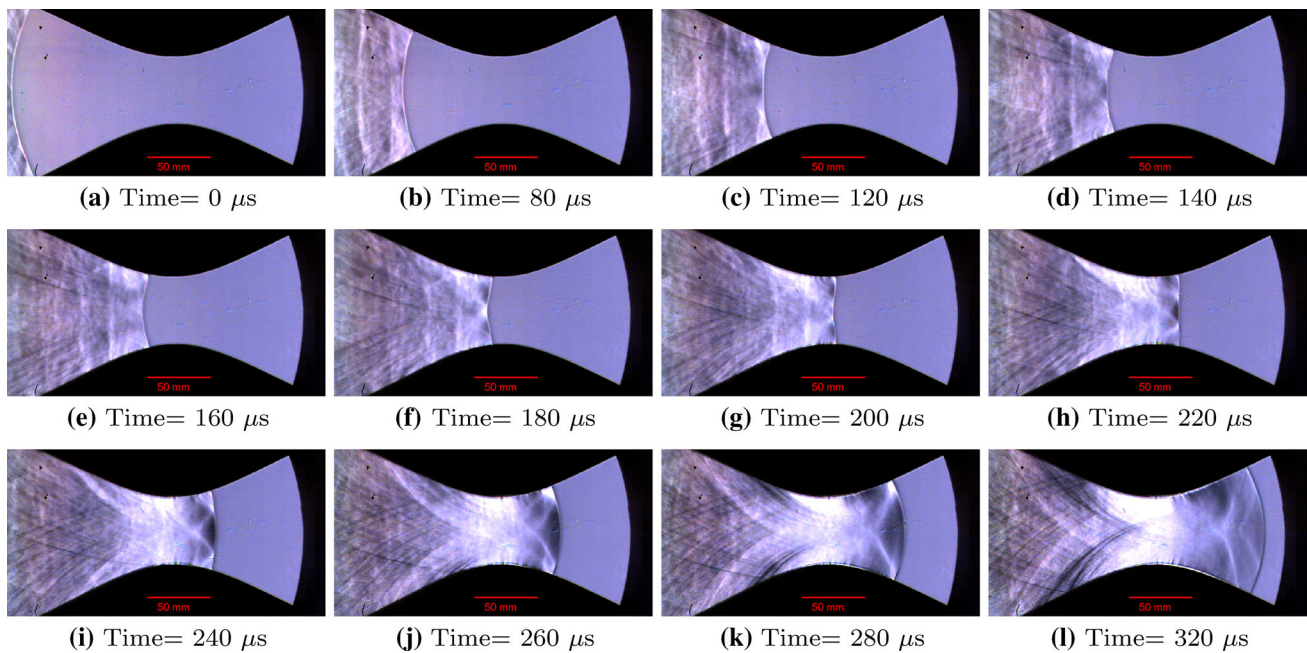


Fig. 14 Propagation of a shock with an initial shock Mach number of 1.30 in a channel with hybrid walls

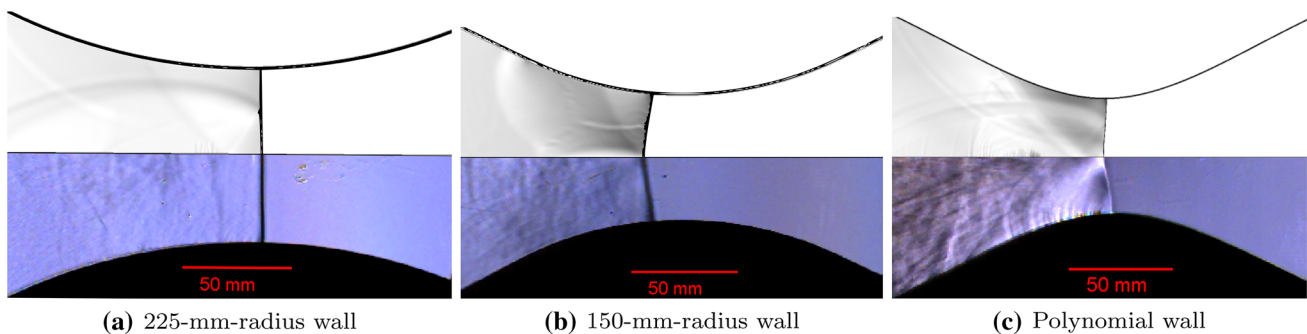


Fig. 15 Comparison between CFD and experimental results at 140 μ s, 200 μ s, and 160 μ s, respectively

was necessary to zoom into the images in order to estimate shock position. The consequence of zooming in was that the shock's thickness was magnified making the shock's location uncertain within the bounds of shock thickness. This uncertainty in shock position translates into errors in the shock's Mach number.

Upon zooming in, the shock has a thickness of 3.8 mm. The scale of the zoomed-in images to the laboratory distances was 123.1 mm: 58.07 mm, implying a shock thickness of 1.75 mm. Shock position (i.e., p_i) was measured at the centre of the zoomed-in shock so that the shock position can be stated as: $p_i \pm \epsilon_p$ where $\epsilon_p = 0.9$ mm (one significant figure).

If we assume that the error in time and temperature measurements are negligible compared to position measurements, then the resulting shock Mach number is given as:

$$M = \frac{p_{i+1} - p_{i-1}}{2a_0\Delta t} \quad (13)$$

using the central difference method. The propagated error in this calculation is then given as:

$$\epsilon_M = \frac{\sqrt{\epsilon_p^2 + \epsilon_p^2}}{2a_0\Delta t} \quad (14)$$

For example, with $\Delta t = 0.02$ s and $c = 342.48$ s (here c is the speed of sound ahead of the shock), the associated error in shock Mach number is: $\epsilon_M = 0.165$ or 0.2 (one significant figure).

5.5 GSD results

Henshaw et al.'s [9] method of solving Whitham's equation was used. The experimental results in Sect. 5.2 were used to define the shock's initial Mach number and shape. It was assumed that the shock's shape is still cylindrical when it is first observed in the experimental images.

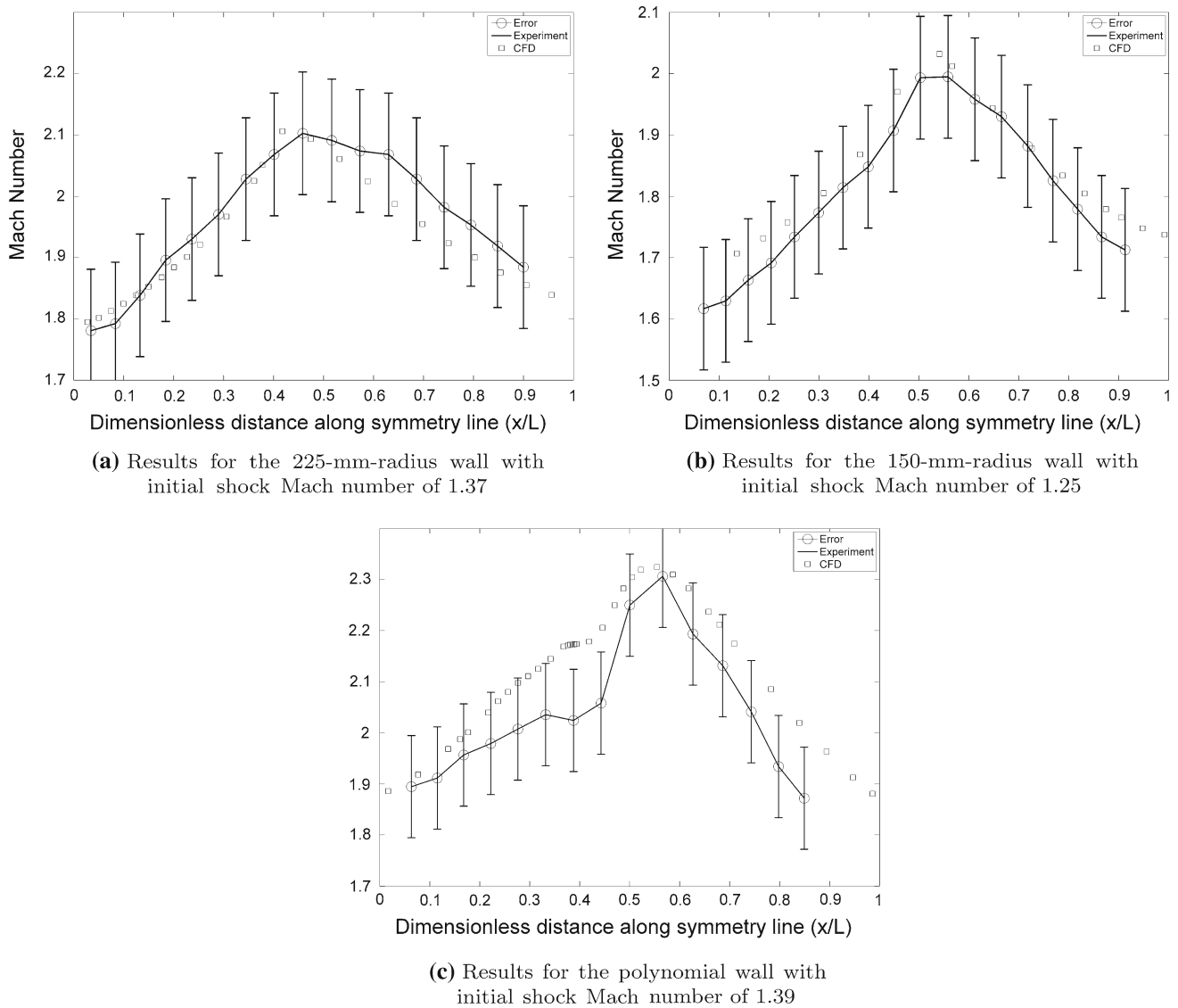


Fig. 16 Comparison of centreline shock Mach number for experimental and CFD results

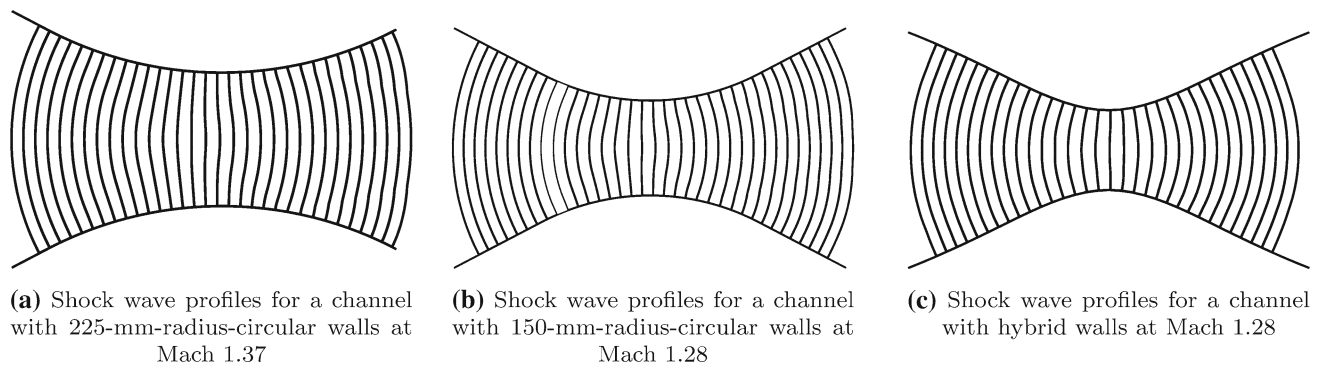


Fig. 17 Shock profiles calculated using Whitham’s GSD

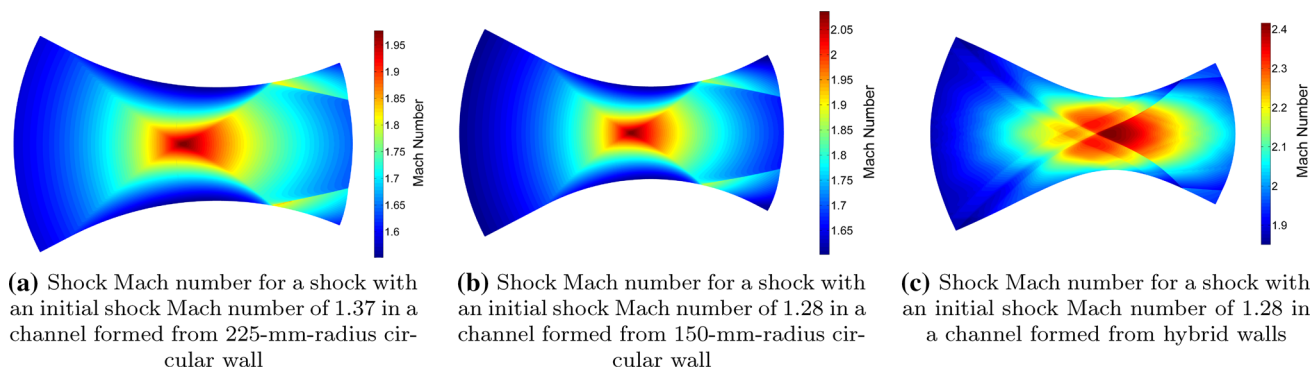


Fig. 18 Shock Mach number variations within the channels as calculated using GSD

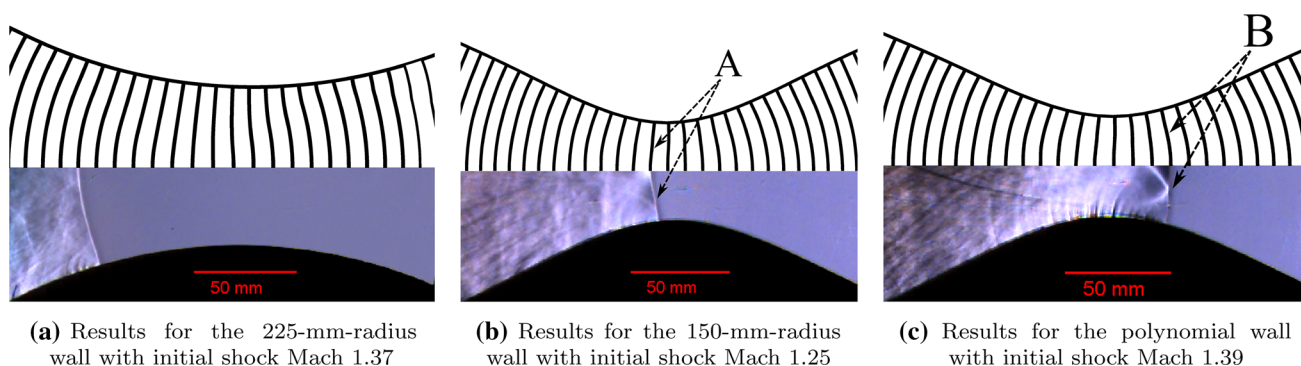


Fig. 19 Experimental shock profiles compared to GSD shock profiles

In the experimental images, the shock thickness makes it difficult to discern shock curvatures. This weakness is not existent in the numerical solution as is seen in Fig. 17; note that the time between discrete profiles is $12.5 \mu\text{s}$. In these numerical profiles, the cylindrical shocks show the partition of the shock front into three portions (the central region between two diffracted portions). Furthermore, the three portions are maintained beyond the channel throat, albeit with gradual smoothing.

Even more expressive are the plots of the shock Mach number variations within the channel (Fig. 18). The plots show the shock Mach numbers frozen in time. In Fig. 18a–c, tracks can be seen radiating from the channel throat's centre towards the walls. These correspond to the multi-wave system observed in Fig. 11e and its propagation towards the walls. Thus, while GSD ignores post-shock conditions, a shock Mach number plot allows for those conditions to be inferred.

In addition, the shock Mach number variation plots help reinforce the mechanism causing the variation in shock profile shape. The shock's Mach number (initially uniform) becomes non-uniform as the shock moves in, towards the throat. It reaches a peak close to the channel throat (along the centreline) and minimum shock Mach number at the walls. This is consistent with a shock front with expansion waves

propagating up and down along it with the centre portion converging towards the focal point.

Figure 18c shows a more complex pattern, with several waves emanating from the walls at the channel entrance. We recall that Fig. 18c corresponds to hybrid walls with both concave and convex walls. Therefore, the tracks correspond to the compressive disturbance waves produced by the concave walls.

The results above illustrate that there is good correlation between GSD and experiment from a qualitative perspective. That is, using GSD, one can infer the pertinent mechanism and estimate shock front shape and evolution thereof.

5.6 Comparison between GSD and experimental results

Figure 19 shows a comparison between GSD and experimental profiles for the three profiles investigated. Overall, the shock profiles from both methods are reasonably similar to each other. However, a slight difference in curvature can be seen at points A and B of Fig. 19b, c, respectively. Presumably, that difference is as a result of the number of points used to discretise the shock in GSD.

Centreline shock Mach numbers from both GSD and experiment were plotted together in Fig. 20a–f. In all cases,

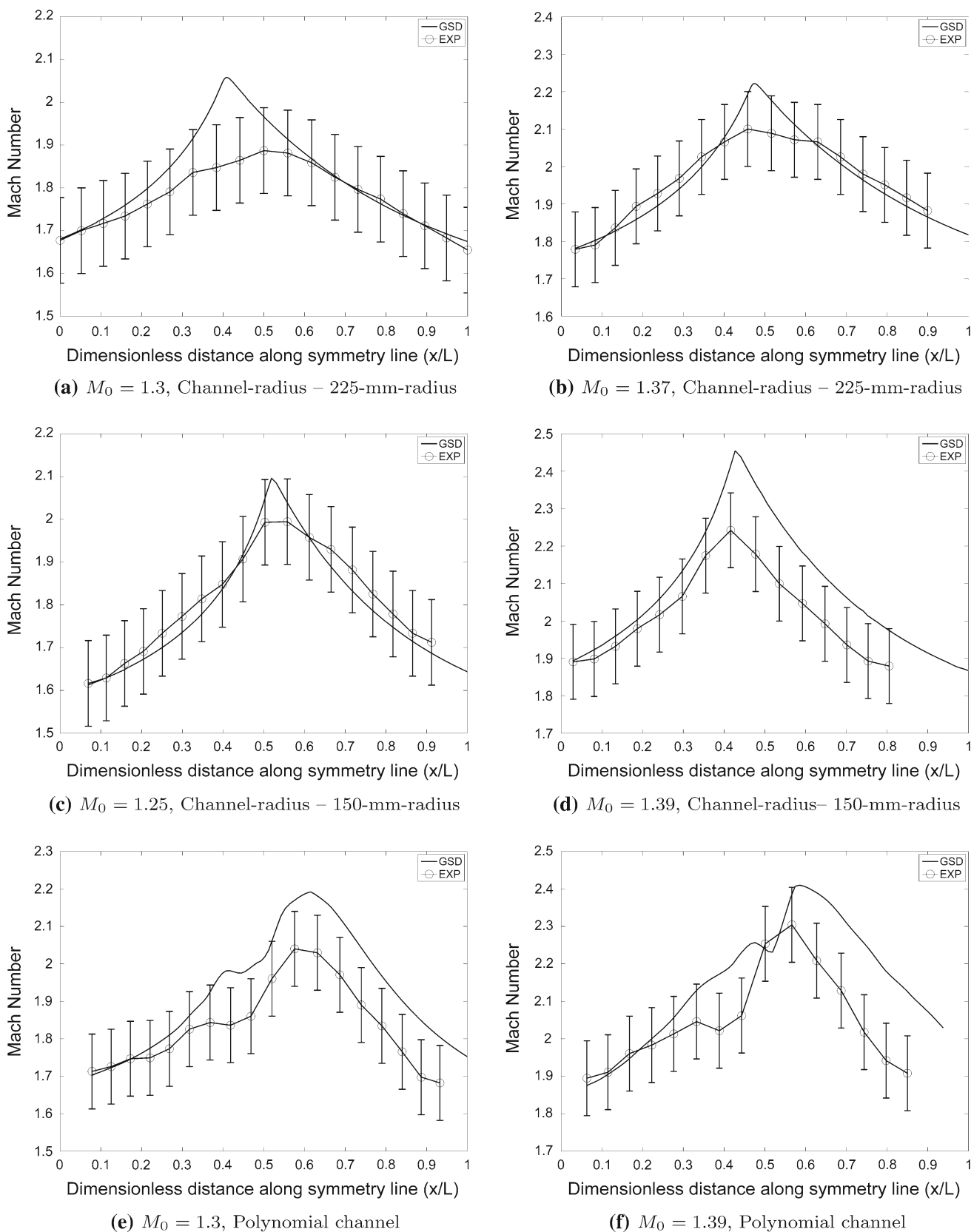


Fig. 20 Comparisons of centreline shock Mach numbers between that calculated using GSD and measured in experiments

GSD predicts a higher peak shock Mach number than is observed in experiments. However, variation in centreline shock Mach number along the channel follows a similar pattern in both GSD and experiments. This is consistent with the qualitative view that the mechanisms concerned are well described by GSD.

As was alluded to in Sect. 2, the change in shock Mach number is communicated by disturbance waves sent from the wall. Further, these disturbance waves propagate at a finite speed. It follows, therefore, that prior to the arrival of the disturbance waves, the shock front should continue to behave as the original cylindrical shock front. This is well modelled by Whitham's theory and exact correspondence between experiment, and the theory was expected in the inlet section of the channel. Allowing for experimental error, this correspondence is seen in Fig. 20.

Figure 20a–d illustrates an accelerating shock front with a peak at the throat and deceleration thereafter. Both GSD and experiment show that the shock front experiences two peaks. This can be understood by reference to the walls that define the channel. In Fig. 20e, f, the channel is defined by hybrid walls, and as has been alluded to, they result in compressive and expansive disturbance waves in the concave and convex wall sections, respectively. It is the arrival of the latter that causes the centreline shock Mach number to briefly drop, resulting in the first peak. Further reductions in channel cross-sectional area lead to further shock acceleration until the second peak.

While the channel is symmetric about the throat, the shock's behaviour is not. After passing through the throat, the centreline shock Mach number does not exhibit the same double peak as was observed in the converging portion; instead, the shock's Mach number monotonically decreases. This illustrates the dominance of area increase over the walls' profiles.

As far as these results show, there still remains quantitative differences between Whitham's GSD and experiment. This is despite the modifications introduced by Milton and Itoh et al. However, in conjunction with Figs. 17 and 18, GSD can be useful in estimating the evolution of a cylindrical shock in a converging–diverging channel.

Aside from the discussion above, a more subtle but potential explanation for the discrepancies observed could be the assumption that the shock and the wall are always perpendicular to each other. This may be true for inviscid flow, but not sound for the case considered here. Consider Figs. 13o, p and 14o, p which show a well-developed boundary layer behind the shock. The boundary layer introduces either a negative or positive displacement, depending on whether the wall is concave or convex, which results in a displaced effective wall. This will have the effect of altering the perpendicularity assumption to some other value [14].

6 A comment on CFD and GSD

Between CFD and GSD results, we observe that the former has better correlation to experimental data, especially for the circular profiles (consider Fig. 16a, b vs. Fig. 20). The polynomial profile, on the other hand, exhibits similar discrepancies in both CFD and GSD (Fig. 16c vs. Fig. 20c). Qualitatively, both methods produce the same centreline Mach number variation: a monotonic acceleration interrupted by a plateau up to a peak and then a monotonic deceleration. Quantitatively, CFD and GSD consistently predict higher centreline Mach numbers, as has already been discussed. However, CFD results are within the experimental data error bounds, except in the plateau region. In comparing the two methods, it must be borne in mind that CFD solves for the complete fluid domain, while GSD primarily accounts for the shock front (in spite of the Itoh et al. modifications).

7 Conclusion

The propagation of two-dimensional cylindrical shock wave segments in converging–diverging channels was experimentally and numerically investigated. The numerical investigation was conducted from a geometric shock dynamics perspective using Whitham's theory and CFD. In general, the subsequent shock front evolution was observed to be dependent on the geometry of the walls defining the channel. With circular walls, expansive disturbance waves were inferred in experimental observations and, to an extent, confirmed by the numerical method. A multi-wave system, similar to a Mach reflection configuration, was observed at the channel throat. Because of channel symmetry, this multi-wave system was observed in both the top and bottom halves of the channel, and this system propagated along the shock front until it reflected off the channel walls; however, one of the multi-wave system's elements did not reflect off the wall, implying that they are different phenomena.

Comparisons between numerical and experimental data showed good qualitative correlation. The calculated shock profiles were similar to those captured in experiments; furthermore, the subtle curvatures of the disturbed portions of the shock front were clarified by thin calculated shock fronts. A plot of shock Mach numbers frozen in time showed what seemed like weak discontinuities in the experimental images. Nevertheless, while qualitative correspondence was good, quantitatively, GSD consistently produced higher shock Mach numbers than were measured in experiments.

Funding Funding was provided by the South African National Research Foundation.

References

1. Edwards, D., Fearnley, P., Nettleton, M.: Shock diffraction in channels with 90° bends. *J. Fluid Mech.* **132**, 257–270 (1983). <https://doi.org/10.1017/S0022112083001597>
2. Chester, W.: The quasi-cylindrical shock tube. *Lond. Edinb. Dublin Philos. Mag. J. Sci.* **45**(371), 1293–1301 (1954). <https://doi.org/10.1080/14786441208561138>
3. Chisnell, R.: The motion of a shock wave in a channel, with applications to cylindrical and spherical shock waves. *J. Fluid Mech.* **2**(3), 286–298 (1957). <https://doi.org/10.1017/S0022112057000130>
4. Whitham, G.: A new approach to problems of shock dynamics Part I. Two-dimensional problems. *J. Fluid Mech.* **2**(2), 145–171 (1957). <https://doi.org/10.1017/S002211205700004X>
5. Skews, B.: The shape of a diffracting shock wave. *J. Fluid Mech.* **29**(2), 297–304 (1967). <https://doi.org/10.1017/S0022112067000825>
6. Bryson, A.E., Gross, R.W.F.: Diffracting of strong shocks by cones, cylinders, and spheres. *J. Fluid Mech.* **10**(1), 1–16 (1961). <https://doi.org/10.1017/S0022112061000019>
7. Milton, B.E.: Mach reflection using ray shock theory. *AIAA J.* **13**, 1531–1533 (1975). <https://doi.org/10.2514/3.60566>
8. Itoh, S., Okazaki, N., Itaya, M.: On the transition between regular and Mach reflection in truly non-stationary flows. *J. Fluid Mech.* **108**, 383–400 (1981). <https://doi.org/10.1017/S0022112081002176>
9. Henshaw, W.D., Smyth, N.F., Schwendeman, D.W.: Numerical shock propagation using geometrical shock dynamics. *J. Fluid Mech.* **171**, 519–545 (1986). <https://doi.org/10.1017/S0022112086001568>
10. Guderley, G.: Starke kugelige und zylindrische Verdichtungsstöße in de Nähe des Kugelmittelpunktes bzw de Zylinderachse. *Luftfahrtforschung* **19**, 128–129 (1942)
11. Roache, P.J.: Perspective: A new method for uniform reporting of grid independence studies. *J. Fluids Eng.* **116**(3), 405–413 (1994). <https://doi.org/10.1115/1.2910291>
12. Lacovig, L.: The construction and calibration of a shock tube for large scale diffraction studies, MSc Dissertation. University of the Witwatersrand (2011)
13. Skews, B., Gray, B., Paton, R.: Experimental production of two-dimensional shock waves of arbitrary profile. *Shock Waves* **25**(1), 1–15 (2015). <https://doi.org/10.1007/s00193-014-0541-4>
14. Shirouzu, M., Glass, I.I.: An assessment of recent results on pseudo-stationary oblique shock wave reflections. UTIAS Report No. 264. University of Toronto, Institute of Aerospace Studies (1982)

Publisher's Note Springer Nature remains neutral with regard to jurisdictional claims in published maps and institutional affiliations.